Radio and Hard X–ray Images of High–Energy Electrons in an X-class Solar Flare

S. M. White[1], S. Krucker[2], K. Shibasaki[3], T. Yokoyama[3], M. Shimojo[3] and M. R. Kundu[1]

ABSTRACT

We present the first comparison between radio images of high–energy electrons accelerated by a solar flare and images of hard X–rays produced by the same electrons at photon energies above 100 keV. The images indicate that the high–energy X–rays originate at the footpoints of the loops dominating the radio emission. The radio and hard X–ray light curves match each other well and are quantitatively consistent with an origin in a single population of nonthermal electrons with a power law index of around 4.5–5. The high-frequency radio spectral index suggests a flatter energy spectrum but this is ruled out by the X–ray spectrum up to 8 MeV. The preflare radio images show a large hot long–lived loop not visible at other wavelengths. Flare radio brightness temperatures exceed 10^9 K and the peak in the radio spectrum is as high as 35 GHz: both these two features and the hard X–ray data require very high densities of nonthermal electrons, possibly as high as 10^{10} cm^{-3} above 20 keV at the peak of the flare.

Subject headings: Sun: flares – Sun: corona – Sun: radio radiation

1. INTRODUCTION

The launch of the Ramaty High Energy Solar Spectroscopic Imager (RHESSI), with its ability to image flares in hard X–rays (HXR) and γ–rays at arcsecond resolution, offers us the opportunity to compare the emissions from electrons in the same energy range at two very different wavelength regimes: hard X–rays (bremsstrahlung) and radio (gyrosynchrotron). Both of these emissions are produced by nonthermal electrons with energies in excess of 100 keV, yet the emission mechanisms have very different properties and offer information on different aspects of conditions in the solar atmosphere. Bremsstrahlung is produced by collisions and therefore requires high densities:

[1]Astronomy Department, University of Maryland, College Park, MD 2074 2

[2]Space Sciences Laboratory, University of California, Berkeley CA 94720-7450

[3]Nobeyama Radio Observatory, NAO, Minamisaku, Nagano 384-13, Japan

in most cases hard X–rays above 100 keV arise from nonthermal electrons striking the chromosphere and images show us the footpoints of the coronal loops carrying the accelerated electrons. Gyrosynchrotron radio emission is produced by the gyromotion of electrons as they travel along coronal magnetic fields. This mechanism is extremely efficient and allows us to detect electrons with energies of hundreds of keV even in very small flares. On the other hand, flares in which X–rays above 100 keV can be imaged are rare because the steeply falling power law spectra do not yield sufficient photons at high energies for image formation.

Most previous comparisons of HXR and radio images involve hard X–rays below 50 keV whose source is dominated by electrons with energies much lower than those that typically produce the nonthermal radio emission. Frequently it is found that the two populations of nonthermal electrons seem to have different energy spectra, implying that they have different origins (e.g., Kundu et al. 1994; Silva et al. 2000). Early comparisons of radio and HXR images were carried out by Hoyng et al. (1983) and Kundu (1984). The largest study comparing radio and HXR images of flares has been carried out by Nishio et al. (1997,2000), who analyzed radio and HXR emission from 25 flares. The excellent RHESSI data for the 2002 July 23 X4.5 flare allow us to make images at hard X-ray energies above 100 keV and compare these with simultaneous radio images of the nonthermal electrons at energies that produce the high energy photons. Radio images of this event from the Nobeyama Radioheliograph (NoRH) have a spatial resolution and temporal cadence that are well matched to the RHESSI data and provide a complementary view of the electrons accelerated by this flare.

2. THE OBSERVATIONS

NoRH observes the Sun at 17 and 34 GHz. The cleaned radio images used here are restored with beams of $10''$ at 17 GHz and $8''$ at 34 GHz. We compare these data with 12–20 keV and 100–150 keV hard X–ray images from RHESSI (made using grids 3 to 8 and reconstructed with $7''$ resolution), and with 195 Å images from the Transition Region and Coronal Explorer (TRACE) satellite. The 195 Å passband of TRACE is dominated by an Fe XII line formed at 1–2 $\times$ 10^6 K, but also contains an Fe XXIV line at 192.03 Å (formed at 10-20 $\times$ 10^6 K) that is usually much weaker (Handy et al. 1999). Images at different wavelengths are coaligned to within about $5''$ using common features.

The radio and HXR time profiles of the event are compared in Figure 1. The radio data are 35 GHz fluxes from the Nobeyama Radio Polarimeters (NoRP), which we compare with the 60–100 keV HXR light curve from RHESSI. The structure of the 35 GHz light curve is representative of all radio frequencies above 4 GHz, and 60–100 keV is representative of the light curves for all hard X–rays above 30 keV; below 30 keV the X–rays show less temporal fine structure in their

light curves (Holman et al. 2003).

The main impulsive phase begins at 00:27:25, but the first sign of an increase in radio emission is at 00:22, when the soft X–rays (< 10 keV) also begin to rise. Harder X–rays (> 40 keV) don't start to rise until 00:26 UT, when the radio emission also shows a step increase. The impulsive phase consists of a number of spikes and dips that are all seen in both the radio and HXR light curves. Different peaks have relatively different heights at the two wavelengths, but over the ≈ 20 minutes of the impulsive phase the similarity in time profiles is striking, including the brief sharp dip at 00:30:20.

Radio fluxes as a function of time at the frequencies 1.0, 2.0, 3.8, 9.4, 17, 35 and 80 GHz are available from NoRP. The lower panel in Fig. 1 represents the spectral evolution of the radio emission using two parameters: the peak frequency, and the radio spectral index from 35 to 80 GHz, converted to the equivalent electron energy spectral index. The peak frequency in the spectrum, i.e., the frequency at which the radio flux is largest at any time, represents the boundary between optically thick low frequency emission and optically thin high frequency emission. The peak frequency shown in Fig. 1 is determined by fitting a parabola to the logarithm of the flux values at the three frequencies closest to the peak. This is equivalent to fitting a gaussian function to the peak in the data. The spectral peaks are very broad and not well fit by either the gaussian or by 4– (Staehli et al. 1989) or 5–parameter (NoRP software routine norp_alpha) representations of a theoretical gyrosynchrotron spectrum.

Away from the impulsive phase, the peak frequency determined in this way is usually close to 10 GHz, but between 00:27:30 and 00:33:00, the peak frequency is much higher, reaching to over 35 GHz at the onset of the impulsive phase and after the large dip at 00:30:20. The 35 GHz flux exceeds the 17 GHz flux in this period. 35 GHz is a very large value for the peak frequency, which more typically is 7–10 GHz for solar radio bursts (Guidice & Castelli 1975; Staehli et al. 1989, 1990). Further, it is unusual for the peak frequency to change during a given event by such a large amount as it does here (e.g., see the discussion by Belkora 1997).

In the course of the analysis of this event, the NoRP staff realized that the NoRP 80 GHz flux measurements reported since about 1992 appear to be too low by a factor of about 6.5 (T. Yokoyama & H. Nakajima, private communication). With the revised 80 GHz fluxes the 35 to 80 GHz spectral index α is found to be quite flat, between -1.6 and -0.8. We adopt the Dulk & Marsh (1982) gyrosynchrotron approximation $\alpha \approx 1.22 - 0.90\delta$ to convert α into an electron energy power law index δ (with $d^2N(E)/dEdV \propto E^{-\delta}$), and find $\delta = 2.7$ to 1.8. However, when the peak frequency is very high as it is for much of this event, the 35 to 80 GHz slope is flatter than the true optically thin slope and δ will be underestimated. An additional complication is that the broad nature of the peak in the spatially-integrated radio spectrum suggests that discrete individual components with a wide range of peak frequencies are present, complicating the interpretation of

the high–frequency spectral index even when the integrated spectrum has a lower peak frequency. We believe that the true value of δ is larger than the 35–to–80 GHz value shown in Fig. 1 for most of the event. For comparison the HXR spectral index from 100–400 keV converted to an electron energy spectral index assuming thick target emission is also plotted (see below).

3. SOURCE MORPHOLOGY

Preflare conditions are shown in panels (a,b) of Figure 2. While the EUV image shows nothing remarkable, the radio image is quite extraordinary. For at least an hour prior to the flare, back to 23 UT (dawn at NoRH), an elongated loop structure is visible in both the 17 and 34 GHz images. The loop extends over $80''$ to the north-east. In the 75 minutes prior to the flare the loop does not seem to change shape, nor are there significant changes in brightness. There is one important difference between the 17 and 34 GHz images: the 17 GHz images show a bright compact source at the base of the loop that has no counterpart at 34 GHz, or in the EUV. The peak 17 GHz brightness temperature in this source declines steadily from 7×10^5 K at 23 UT to 2.5×10^5 K at 00:15 UT. The loop has a radio spectrum consistent with optically thin thermal radio emission (brightness temperatures of 100–120 $\times 10^3$ K at 17 GHz and about 1/4 as much at 34 GHz). This loop could be a hot post-flare loop from an earlier event, but if so, it must be at a temperature well above the formation temperature of Fe XII, $\approx 1.5 \times 10^6$ K, and it would be surprising that the loop shows no decline with time, and the EUV images show no signs of plasma from a hot loop cooling into the Fe XII range. The compact 17 GHz peak is undetected in the 34 GHz image and the 17 to 34 GHz brightness temperature ratio is in excess of 6 for this feature and requires a nonthermal emission mechanism. The flare starts at the location of this feature.

Panels (c) and (d) of Fig. 2 show images during flare onset, with important features in the 195 Å image (panel d) labelled in both panels. The linear features in the TRACE image (d) labelled "ribbons" appear to be very low in the atmosphere. The right-hand ribbon is the first flare feature to appear in the 195 Å images, at 00:21:29. The NoRH images show emission starting at 00:21:00 UT, with a faint sign of emission from the ribbon, but with the strongest emission extending from the location of the brightest 17 GHz feature in panel (a) northwards for about $20''$. By 00:22:00 UT, the peak 17 GHz brightness temperature in the right hand ribbon is of order 10^5 K, while it is 10^6 K in the brightest radio source. Both these features would be detected at 34 GHz at this time if the radio emission were due to thermal bremsstrahlung, but the 34 GHz images show no emission. We conclude that the radio emission is nonthermal, and that acceleration to energies of hundreds of keV commenced at 00:21:00 UT even though there is no indication of bremsstrahlung from these electrons in the 60–100 keV light curve at this time.

At the time shown in panels (c,d), 00:24:57, the ribbon is clearly visible in the 195 Å image

(panel d), the 17 (contours in panel c) and 34 GHz radio images and the RHESSI 12–20 keV image (greyscale in panel c). In addition to the western ribbon, the 195 Å image at this time shows a ribbon to the east (arrowed), also low in the atmosphere, as well as what seems to be a high diffuse loop connecting the eastern and western sides of the flare region (arrowed). 34 GHz images at this time are dominated by this loop feature. From the coincidence of the 34 GHz, 12–20 keV and 195 Å images of the bright loop at 00:24:56 and its diffuse appearance, we argue that the TRACE image does not show Fe XII emission from the loop but rather Fe XXIV emission from within the TRACE 195 Å passband. Fe XXIV has a formation temperature of order 10–20 $\times$ 10^6 K, so this loop feature is the first sign of hot soft X–ray emitting plasma.

The 100–150 keV HXR are not strong enough to be imaged until 00:27:45, when they show two compact sources of similar strength separated by about $12''$ along a SE–NW direction (panel e). They are located to the west of the 12–20 keV HXR peak, which still resembles the 195 Å image. The 17 GHz peak brightness temperature has jumped from 6.0 $\times$ 10^6 K at 00:24:57 to 8.5 $\times$ 10^8 K. From this time on the 195 Å images are saturated, but are consistent with an arcade of loops seen in projection close to the limb. As time proceeds the arcade lengthens to the north–east, and the original loops at the western end of the arcade tend to fade. The RHESSI 12–20 keV images are consistent with thermal plasma near the tops of these loops, while the 100–150 keV images continue to show a pair of sources whose separation increases with time (Krucker et al. 2003).

Overall, the 17 GHz radio source does not change its size or morphology greatly from 00:27 to 00:40. Spatially, the peak of the radio emission appears to lie at the top of the arcade of loops seen in the 195 Å images, close to the peak in the 12–20 keV HXR images. The peak brightness temperature in the 17 GHz images reaches 10^9 K at 00:28:00 UT and peaks at 1.4 $\times$ 10^9 K at 00:31:00, after the sharp dip in flux. At this time 17 GHz is on the optically thick side of the spectral peak, so the brightness temperature should represent the mean energy of the electrons contributing most to the 17 GHz flux: 1.4 $\times$ 10^9 K corresponds to a kinetic energy of order 120 keV. The radio polarization in this flare at 17 GHz is relatively weak (several percent), with images consistently showing right circular polarization from the footpoints on the north–western side of the arcade and left circular polarization from the south–eastern side of the arcade.

4. ELECTRON ENERGY DISTRIBUTION

We have fit the RHESSI hard X–ray spectrum from 40 to 400 keV with a broken power law using the SPEX program and find that from 00:28:00 to 00:37:00, the spectrum above 100 keV has a constant slope between -2.9 and -3.1 (in agreement with Holman et al. 2003). Assuming that the slope of -3 represents thick target emission, the corresponding electron energy spectrum has

a power–law slope of $\delta \approx 4.5$. For comparison with the radio data, we calculate the nonthermal number density at the footpoints from the HXR data at 00:35:00 when the radio spectral peak is well below 34 GHz. The 40–400 keV photon energy (E_γ) spectrum at this time has the form $9\,(E_\gamma/50\,\mathrm{keV})^{-3.2}$ photons cm^{-2} keV^{-1} s^{-1}. The corresponding flux of electrons striking the chromosphere is $2 \times 10^{35}(E/20\,\mathrm{keV})^{-4.2}$ electrons (keV s)$^{-1}$ (Hudson et al. 1978). To convert this to a number density we need to divide by the footpoint area A. The RHESSI images do not resolve the footpoints at a resolution of $7''$ and images made using grid 1 suggest a size as small as $2''$. If we adopt $A = 10^{16}$ cm^2, corresponding to a diameter of $2''$, and assume electron energy equipartition between the three directions of motion, we derive an energy distribution for the electron number density at the footpoints of $5 \times 10^9\ (E/20\,\mathrm{keV})^{-4.7}\ (A/10^{16}\,\mathrm{cm}^2)$ electrons cm^{-3} keV^{-1}.

The radio and HXR images indicate that both sources lie on the same field lines, with HXR bright only at the footpoints and the radio brightest at the looptops, so we can compare the two quantitatively despite their differing spatial morphologies. The radio data also require very high densities. Based on gyrosynchrotron theory, the brightness temperatures of over 10^9 K achieved at 17 GHz at the peak of the flare can only be produced by an electron energy spectrum as steep as -4.7 (appropriate at electron energies of 120 keV) if the harmonic number is in excess of 30 (see figures in Dulk & Marsh 1982, confirmed by our own calculations). Such high harmonic numbers imply a relatively small magnetic field strength, no more than 200 G, and to achieve the same radio brightness temperature with the lower value of B, nonthermal densities over 10^{10} cm^{-3} above 20 keV are required, similar to those found above from the HXR data. The low value for B is consistent with the location of the brightest radio emission at the top of the arcade of loops.

However, the energy spectral index derived from the 35 to 80 GHz radio spectra, $\delta \approx 2.6$–1.8, does not agree with the value derived from the 40–400 keV HXR, $\delta \approx 4.5$. The electron energy density distribution derived from the radio data at 00:35 UT if the energy spectral index takes the radio value, 2.5 (Fig. 1), is $5 \times 10^6\ (B/200\,\mathrm{G})^{-2.1}\ (E/20\,\mathrm{keV})^{-2.5}$ electrons cm^{-3} keV^{-1} (34 GHz brightness temperature of 1.8×10^8 K, line–of–sight depth through the source of 5×10^8 cm and an angle between the magnetic field and the line of sight of $\sin^{-1}(0.8)$; Dulk & Marsh 1982). Since the radio and HXR profiles are so similar, we cannot argue that the radio emission comes from a long-lived population of trapped electrons while the hard X–rays come from directly precipitating electrons, as occurs in other events where the time profiles clearly differ (e.g., Raulin et al. 1999): the radio–emitting electrons have the same time behaviour as the hard X–ray emitting electrons and should have a common origin and common evolution. The flat high-energy spectrum derived from the radio spectral index intersects the steep low-energy spectrum derived from the RHESSI data at an electron energy of 1 MeV, and since bremsstrahlung photons are typically just a fraction of the energy of the radiating electrons (Kosugi et al. 1988; Nitta et al. 1991), a calculation shows that the flat spectrum should dominate the X–rays above 100 keV. There is no sign of such flattening in the RHESSI data up to 8 MeV (Smith et al. 2003), so we argue that the radio spectral indices in

Fig. 1 are ruled out by the RHESSI observations. We are forced to assume that the high–frequency radio emission is dominated by a region with a high turnover frequency so that the 35–80 GHz spectrum does not represent optically thin emission, even in the later stages of the flare, and the true optically–thin radio spectral index is steeper than derived above. Nitta et al. (1991) reached a similar conclusion for their event.

5. CONCLUSIONS

Observations of the 2002 July 23 event are consistent with the general picture of nonthermal electrons at energies of many hundreds of keV radiating at radio wavelengths as they travel along the coronal portion of the loop and 100–150 keV HXR when they strike the chromosphere at the footpoints of magnetic field lines. A single population of electrons with a power–law index of about -4.5 to -5 above 100 keV can produce the emission at both wavelengths if we assume that the 35 to 80 GHz radio spectral index does not reflect the true optically–thin value. The radio and HXR light curves show essentially identical structure with many individual peaks, implying a common behaviour. The peak radio brightness temperature of 1.4×10^9 K is one of the highest measurements ever for incoherent emission from a solar flare. The peak frequency in the radio spectrum also achieves very high values of up to 35 GHz.

Prior to the flare the radio images show a highly distended loop, rooted in the eventual flare site, that is not visible at other wavelengths investigated and is very stable. The flare starts with ribbons low in the atmosphere that are visible at radio, X–ray and EUV wavelengths, and expands to fill an arcade of magnetic field lines with nonthermal particles.

Quantitatively the data for this event provide a challenge for our understanding of flares. Both radio and HXR data require extreme number densities of nonthermal electrons to be accelerated in the energy release: over 10^{10} cm^{-3} above 20 keV. Even higher densities must be present in the parent population from which this nonthermal population was accelerated. The corresponding energy densities are substantial: 300 ergs cm^{-3} above 20 keV, while the energy density in the 200 G coronal magnetic field is of order 2000 ergs cm^{-3}. The peak thermal energy density (10^{11} cm^{-3} at 35 MK Holman et al. 2003) is of order 500 ergs cm^{-3}. These numbers imply an acceleration mechanism of very high efficiency.

This research was supported by NSF grants ATM 99-90809 and INT-98-19917, and NASA grants NAG 5-8192 and NAG 5-10175. We thank John Brown, Brian Dennis, Gordon Holman and Hugh Hudson for their comments on the manuscript.

REFERENCES

Belkora, L. 1997, Astrophys. J., 481, 532

Dulk, G. A. & Marsh, K. A. 1982, Astrophys. J., 259, 350

Guidice, D. A. & Castelli, J. P. 1975, Solar Phys., 44, 155

Handy, B. N., Acton, L. W., Kankelborg, C. C., et al. 1999, Solar Phys., 187, 229

Holman, G. D., Sui, L., Schwartz, R. A., & Emslie, A. G. 2003, Astrophys. J. (Lett.), submitted

Hoyng, P., Marsh, K. A., Zirin, H., & Dennis, B. R. 1983, Astrophys. J., 268, 865

Hudson, H. S., Canfield, R. C., & Kane, S. R. 1978, Solar Phys., 60, 137

Kosugi, T., Dennis, B. R., & Kai, K. 1988, Astrophys. J., 324, 1118

Krucker, S., Hurford, G. J., & Lin, R. P. 2003, Astrophys. J. (Lett.), submitted

Kundu, M. R. 1984, Adv. Space Res., 4, 157

Kundu, M. R., White, S. M., Gopalswamy, N., & Lim, J. 1994, Astrophys. J. Supp., 90, 599

Nishio, M., Kosugi, T., Yaji, K., Nakajima, H., & Sakurai, T. 2000, Advances in Space Research, 25, 1791

Nishio, M., Yaji, K., Kosugi, T., Nakajima, H., & Sakurai, T. 1997, Astrophys. J., 489, 976

Nitta, N., White, S. M., Schmahl, E. J., & Kundu, M. R. 1991, Solar Phys., 132, 125

Raulin, J., White, S. M., Kundu, M. R., Silva, A. R., & Shibasaki, K. 1999, Astrophys. J., 522, 547

Silva, A. V. R., Wang, H., & Gary, D. E. 2000, Astrophys. J., 545, 1116

Smith, D. M., Share, G. H., Murphy, R. J., Schwartz, R. A., Shih, A. Y., & Lin, R. P. 2003, Astrophys. J. (Lett.), in press

Staehli, M., Gary, D. E., & Hurford, G. J. 1989, Solar Phys., 120, 351

—. 1990, Solar Phys., 125, 343

This preprint was prepared with the AAS LaTeX macros v5.0.

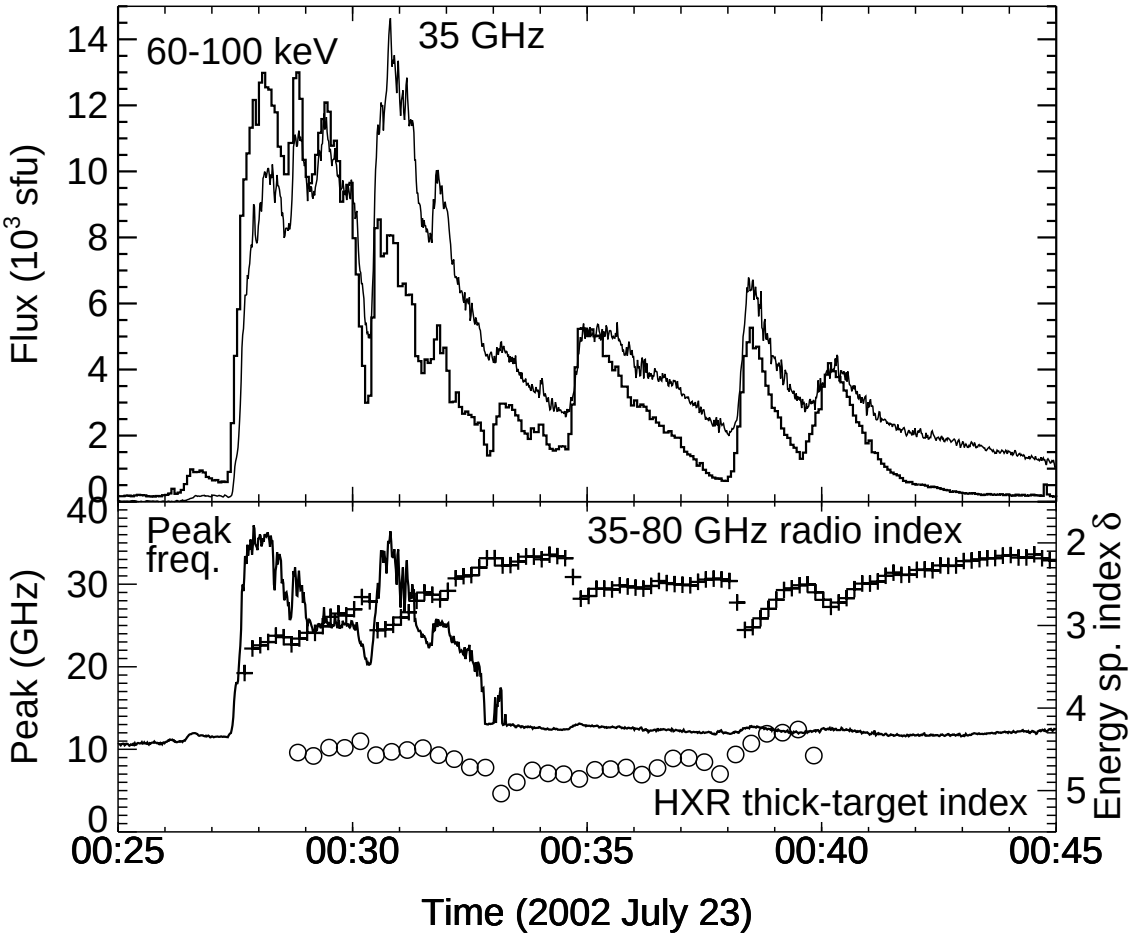

Fig. 1.— Comparison (upper panel) of the RHESSI 60–100 keV hard X-ray light curve (histogram) and the NoRP 35 GHz light curve (solid curve), as well as (lower panel) the time evolution of the radio spectral peak frequency (solid line) and the radio spectral index from 35 to 80 GHz converted to an electron energy spectral index assuming optically thin gyrosynchrotron emission (plus symbols, uncertainty ± 0.3). For comparison, the thick target electron energy index obtained from the RHESSI 100–400 keV spectrum is also shown (open circles; formal uncertainty ± 0.2).

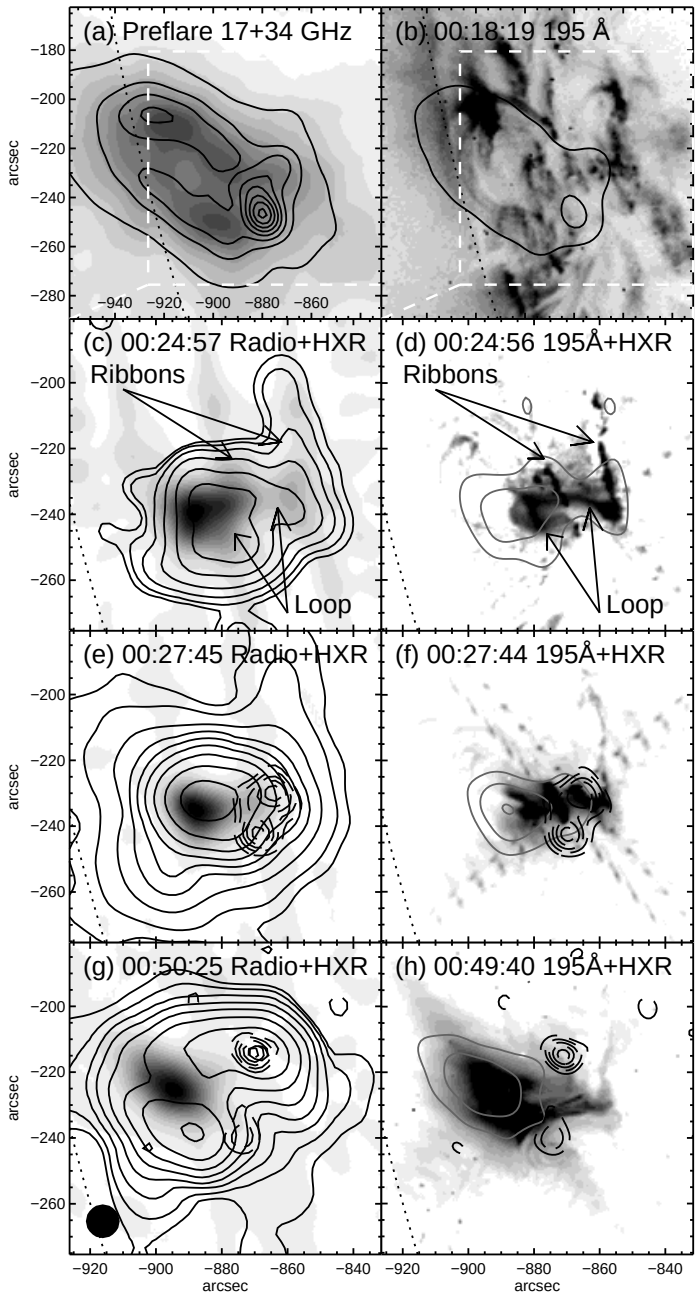

Fig. 2.— Images of the flare at X-ray, EUV and radio wavelengths. The top row of panels shows radio and EUV images in the preflare phase. On the left are 17 GHz contours overlaid on a greyscale 34 GHz image (both averaged over the period 23:00–00:15 UT), while the right panel shows the 195 Å image from 00:18:19 UT together with two 17 GHz contours for context. The remaining rows of panels show the $96'' \times 96''$ region outlined in the preflare images. The left panels show the RHESSI greyscale image of 12–20 keV HXR overlaid with 17 GHz total intensity radio contours (solid) and RHESSI 100–150 keV HXR contours (dashed), while the right panels show a 195 Å image of the same region overlaid with solid grey contours for the RHESSI 12–20 keV HXR and dashed black contours for the RHESSI 100–150 keV HXR. The panel labels refer to the times of the 17 GHz images (left) and the TRACE images (right). Contours for the 17 GHz and 12–20 keV images are at powers of e times $4 \times$ the noise level in the respective images. The 100–150 keV contours are at 3,5,7,9,... times the noise level. The 17 GHz restoring beam size of $10''$ is shown in panel (g); in panel (c) the preflare 17 GHz image (panel a) has been subtracted from the image shown in contours to emphasize the changes.